

Dynamic distinctions in the sodium-calcium exchanger adopting the inward- and outward-facing conformational states

Moshe Giladi^{1,2}, Liat van Dijk¹, Bosmat Refaeli¹, Lior Almagor¹, Reuben Hiller¹,
Petr Man^{3,4}, Eric Forest^{5,6,7}, and Daniel Khananshvili¹

¹Department of Physiology and Pharmacology, Sackler School of Medicine, Tel-Aviv University, Ramat-Aviv 69978, Israel.

²Tel-Aviv Sourasky Medical Center, Tel-Aviv, Israel.

³BioCeV - Institute of Microbiology, Academy of Sciences of the Czech Republic, Prague, Czech Republic.

⁴Faculty of Science, Charles University, Prague, Czech Republic.

⁵Univ. Grenoble Alpes, IBS, F-38044 Grenoble, France.

⁶CNRS, IBS, F-38044 Grenoble, France.

⁷CEA, IBS, F-38044 Grenoble, France.

Running title: *Conformational dynamics of the NCX transporter*

To whom correspondence should be addressed: Prof. Daniel Khananshvili, Department of Physiology and Pharmacology, Sackler School of Medicine, Tel-Aviv University, Ramat-Aviv, Tel-Aviv 69978, Israel, Tel: 972-3-640-9961; Fax: 972-3-640-9113; E-mail: dhanan@post.tau.ac.il

Keywords: NCX, conformational dynamics, alternating access, HDX-MS, ion binding sites, two-fold asymmetry, transporter, antiporter, calcium-transporting protein

ABSTRACT

Na⁺/Ca²⁺ exchanger (NCX) proteins operate through the alternating access mechanism, where the ion-binding pocket is exposed in succession either to the extracellular or the intracellular face of the membrane. The archaeal NCX_Mj (*Methanococcus jannaschii* NCX) system was used to resolve the backbone dynamics in the inward-facing (IF) and outward-facing (OF) states by analyzing purified preparations of apo and ion-bound forms of NCX_Mj-WT and its mutant, NCX_Mj-5L6-8. First, the exposure of extracellular and cytosolic vestibules to the bulk phase was evaluated as the reactivity of single cysteine-mutants to a fluorescent probe, verifying that NCX_Mj-WT and NCX_Mj-5L6-8 preferentially adopt the OF and IF states, respectively. Next, hydrogen-deuterium exchange mass-spectrometry (HDX-MS) was employed to analyze the backbone dynamics

profiles in proteins, preferentially adopting the OF (WT) and IF (5L6-8) states either in the presence or absence of ions. Characteristic differences in the backbone dynamics were identified between apo NCX_Mj-WT and NCX_Mj-5L6-8, thereby underscoring specific conformational patterns owned by the OF and IF states. Saturating concentrations of Na⁺ or Ca²⁺ specifically modify HDX patterns, revealing that the ion-bound/occluded states are much more stable (rigid) in the OF than in the IF state. Conformational differences observed in the ion-occluded OF and IF states can account for diversifying the ion-release dynamics and apparent affinity (K_m) at opposite sides of the membrane, where specific structure-dynamic elements can effectively match the rates of bidirectional ion movements at physiological ion concentrations.

Membrane transporters undergo an alternative exposure of substrate-binding sites at opposite sides of the membrane,

while adopting at least two major conformational states, assigned as the inward-facing (IF) and outward-facing

(OF) states (1-3). In agreement with this dogma, extensive crystallographic studies have identified the OF, IF, and occluded states for many transporters (3-5), but the dynamic features of alternative OF/IF shuttling remain unclear even for proteins with a known crystal structure. The emerging challenge is to identify and characterize the conformational states that govern the rate-equilibrium features of substrate-coupled alternating access. The physiological significance of these issues is difficult to underestimate since the underlying mechanisms might govern the apparent affinity of substrate binding, the turnover rates of the transport cycle, and the intrinsic asymmetry of bidirectional ion movements, among others (5-7).

$\text{Na}^+/\text{Ca}^{2+}$ exchanger (NCX) proteins transport cytosolic and organelle Ca^{2+} and thereby play a key role in Ca^{2+} signaling in health and disease (8-11). The NCX gene family is one of five gene families belonging to the Ca^{2+} /cation exchanger superfamily (11-13), which share common structural features with inverted twofold pseudo-symmetry (14-18). NCXs use the electrochemical gradient of $[\text{Na}^+]_i$ to extrude 1Ca^{2+} in exchange with 3Na^+ (19,20), where the Na^+ - and Ca^{2+} -bound species are transported in separate steps (21,22). The ion-transport rates vary over 10^3 -fold among NCX orthologs, isoforms, and their splice variants since the Ca^{2+} -extrusion rates in a given cell type must match the cell-specific dynamic swings in the cytosolic Ca^{2+} levels (23-25).

NCX from *Methanococcus jannaschii* (NCX_Mj) was crystallized in several states, representing the open, semi-open, and occluded states in the OF orientation (14,26). The crystal structures contain ten helices arranged as two pseudo-symmetrical core units (TM1-5 and TM6-10) connected by a short cytosolic loop (5L6) between TM5 and TM6 (Figure 1A-C) (14,26). TM2-5 and TM7-10 are tightly packed and interact with a limply allocated two-helix cluster (TM1 and TM6), assigned as the gating bundle. Twelve conserved ion-

coordinating residues (on TM2, TM3, TM7 and TM8) form four ion-binding sites: S_{ext} , S_{mid} , S_{int} , and S_{Ca} (14,26). Na^+ and Ca^{2+} bind in a mutually exclusive manner, where 3Na^+ ions occupy S_{ext} , S_{Ca} , and S_{int} , whereas Ca^{2+} occupies S_{Ca} (Figure 1D,E) (27). This assignment of ion binding sites was confirmed by crystallographic studies (26). In the semi-open OF state, two Na^+ ions occupy S_{int} and S_{Ca} where the binding of the third Na^+ to S_{ext} results in 3Na^+ occlusion with associated backbone bending between TM7A and TM7B (26) (Figure 1F).

From a mechanistic point of view, it is worthwhile to note that the gating bundle (TM1/TM6) retains its position before and after 3Na^+ occlusion (26). This experimental fact is consistent with a notion that only the transition state stabilization of ion-bound species (between the OF- and IF-occluded states) can induce the movement of the gating bundle toward performing the alternating access (28). In conjunction with the IF crystal structures of $\text{H}^+/\text{Ca}^{2+}$ exchangers (showing striking structural similarities with NCX), a general mechanism of alternative access has been suggested for the Ca^{2+} /cation exchanger superfamily (14-18). According to this proposal the gating bundle (TM1/TM6) slides in front of a rigid eight-helix core upon ion binding, thereby representing the ion-coupled alternating access (14,15,26-28). Although it is widely accepted that the movement of the gating bundle might be a major conformational change during the OF/IF swapping, it remains unclear how ion binding promotes the sliding of the TM1/TM6 cluster. Notably, the ion binding to respective sites can primarily induce very small conformational changes in the backbone dynamics (e.g., by "narrowing" the ion-binding pore), which may induce the sliding of the gating bundle (15). Thus, it is justified to find alternative approaches for identifying and characterizing the primary changes in the backbone dynamics upon ion binding, as intended in the present work.

The inverted twofold *pseudo*-symmetry of NCX_Mj (Figure 1A-C) results in an intrinsic asymmetry in bidirectional ion movements, as previously demonstrated by kinetic analyses (23,28,29). Namely, under steady-state conditions, the membrane-bound NCX_Mj and its mammalian orthologs seem to preferentially adopt the OF state (23,25,28). These kinetic observations are in agreement with the crystallographic structures demonstrating the preferential stabilization of NCX_Mj in the OF (extracellular) state (14,26). This intrinsic asymmetry of bidirectional Ca^{2+} movements is of major physiological relevance, since it can govern the K_m values at opposite sides of the membrane, while retaining physiologically relevant rates of Ca^{2+} transport under the given ionic conditions (30-33). Notably, an elongation of the loop between TM5 and TM6 (5L6) in NCX_Mj, by inserting 8 residues (assigned as the 5L6-8 mutant), reverses the directionality of asymmetry by stabilizing the IF state (23,27). Thus, crystallographic and kinetic data revealed that NCX_Mj-WT preferentially adopts the OF state (14,23,26) whereas in the absence of the crystal structure of NCX_Mj-5L6-8, the kinetic analysis suggests preferential stabilization of NCX_Mj-5L6-8 in the IF state (23).

In the present study, HDX-MS (hydrogen-deuterium exchange mass-spectrometry) has been applied for analyzing the apo- and ion-bound states of purified NCX_Mj-WT and NCX_Mj-5L6-8 proteins with the goal of patterning the local backbone dynamics in the OF (WT) and IF (5L6-8) states. HDX-MS measures the exchange of backbone amide hydrogen with deuterium in solvents in the presence or absence of ligands, whereas more flexible or solvent-exposed regions take up more deuterium than do the rigid or non-exposed regions (34-38). Thus, HDX-MS allows one to estimate not only ligand-induced effects, but also the patterns of local backbone dynamic in the apo state (36-41). The HDX-MS analysis

is the method of choice for analyzing the local backbone dynamics of ion-occluded states, since HDX-MS techniques can detect relatively small and slow conformational changes (35-41). The status of the OF and IF orientation in purified preparations of NCX_Mj-WT and NCX_Mj-5L6-8 were evaluated by covalent labeling of single-cysteine mutants with the highly sensitive fluorescent probe, tetramethylrhodamine-5-maleimide (TMRM maleimide) (42,43).

The most important message from the present study is that the cytosolic and extracellular domains of the NCX_Mj protein exhibit characteristic differences in the backbone dynamics of the cytosolic and extracellular domains when adopting the OF or IF state. These conformational differences, implemented in the OF and IF states, are largely predefined by the apo protein's structure, although Na^+ or Ca^{2+} binding results in relatively small, but specific rigidification of local backbone dynamics at specific segments.

RESULTS

Covalent labeling of NCX_Mj-WT and NCX_MJ-5L6-8 reveals their preferential orientations in solution

To verify that NCX_Mj-WT and NCX_Mj-5L6-8 indeed represent the OF and IF stabilized states and are thus suitable for HDX-MS analysis, we sought to find an independent method to determine the exposure of cytosolic and extracellular vestibules to bulk phase. According to the crystal structure of NCX_Mj and the model of IF NCX_Mj, G42 should be accessible to the bulk phase solution in the IF state and not the OF state, whereas the opposite is true for G201 (Figure 2). To verify the orientations of NCX_Mj-WT and NCX_Mj-5L6-8, four single-cysteine mutants (WT-G42C, WT-G201C, 5L6-8-G42C, and 5L6-8-G201C) were prepared. The accessibility of the introduced cysteines in solution was assessed by their site-directed covalent labeling with the fluorescent probe, TMRM maleimide

(42,43). This approach assumes that specific cysteine residues have a different access to bulk-phase TMRM maleimide when adopting the OF or IF orientation, as reflected by their TMRM maleimide-labeling rate. Notably, NCX_Mj contains two native cysteine residues (C78 and C80) but they are inaccessible to bulk-phase TMRM maleimide. The labeling of WT-G201C by TMRM maleimide is nearly 10 times faster than the labeling of WT-G42C (Figure 2A). In contrast, the labeling of 5L6-8-G201C is at least 5 times slower than the labeling of 5L6-8-G42C (Figure 2B). Thus, the relative accessibility of the intracellular and cytosolic vestibules to the bulk phase (IF/OF) can be experimentally evaluated by measuring the ratios of the G42C and G201C labeling rates (k_{G42C}/k_{G201}) in a given protein. Thus, the rate ratio of 0.11 ± 0.03 for apo-WT refers to the OF stabilization (Figure 2A), whereas the rate ratio of 5.1 ± 0.7 for apo-5L6-8 reveals the IF stabilization (Figure 2B). These data establish that purified apo-WT preferentially adopts the OF state, whereas apo-5L6-8 is favorably stabilized in the IF state. This statement represents a critical conceptual platform for conclusive interpretation of the HDX-MS data (see below), especially in the case of the apo-5L6 protein since the crystal structure of the IF state is unavailable.

HDX-MS sequence coverage

Mass-spectrometric analysis has identified eleven peptides (proteolytic digestion products of NCX_Mj), thereby allowing us to calculate HDX in eleven local regions. The N-terminus amino acid of each peptide was ignored or alternatively, was calculated from the difference between the two overlapping peptides. The observed sequence coverage (26.7%, Figure 3 and Table 1) of NCX_Mj is quite low in comparison with soluble proteins, since the detergent protects the protein from proteolysis and obscures the signal from highly hydrophobic peptides (28). Despite these technical limitations,

the regions of interest (TM2, TM7, and TM8), containing ten out of twelve ion-coordinating residues, are well covered in the present HDX-MS analysis (Figures 2-6). TM2 is covered by three short regions; TM7 and TM8 are covered by 4 regions each; and TM9 is partially covered by one region. TM4-6 and TM9-10 do not contain any ion-binding residues and are not predicted to undergo significant deuterium uptake since they face the membrane, a-priori precluding deuterium uptake (Figure 1A-C). Indeed, in all the examined samples, the region covering TM9 has a very low deuterium uptake in the apo state, which remains unaffected in the presence of ions (Figures 3-6).

Backbone dynamics of apo OF (WT) and IF (5L6-8) NCX_Mj

To study purified proteins in the apo form, Na^+ was replaced by choline (100 mM) and Ca^{2+} was chelated using EDTA (10 mM). Eleven peptide regions have been analyzed after quenching the HDX reaction (Figures 3,4 and Table 1). The deuterium uptake is plotted as a function of time in Figure 4A and as color-coded heat maps on apo OF and IF NCX_Mj in Figure 4B. The deuterium uptake plot of peptide 260-264 is not shown, since as mentioned above, this region is highly protected in all the samples used in this study (Figures 4-6).

The majority of the analyzed peptides exhibit similar deuterium uptake over time in WT and 5L6-8, whereas two peptides, 40-46 and 194-204 (corresponding to regions 41-46 and 195-204, respectively), representing matching counterparts at inverted segments of TM2 and TM7, possess inversed capacities for deuterium uptake (Figure 4). That is, peptide 40-46 (at the cytosolic TM2A region) has lower deuterium uptake in the OF (WT) NCX_Mj, whereas peptide 194-204 (at the extracellular TM7A region) has lower deuterium uptake in the IF (5L6-8) NCX_Mj (Figure 4). The 204-205 region at the TM7A-TM7B hinge (which bends during the transition of the semi-open

state to the occluded state (26) exhibits high deuterium uptake in all samples. In 5L6-8 (but not in WT), TM2A takes up more deuterium than does TM2B, which is consistent with bending of the TM2A-TM2B hinge similar to the bending of the TM7A-TM7B hinge in the OF state.

Interestingly, in the apo state, both WT and 5L6-8 NCX_Mj manifest marked differences in local backbone dynamics among residues involved in ion-transport catalysis (e.g., the 41-59 region on TM2). The 48-52 region at the very center of the ion-binding cluster exhibits very low deuteration in both WT and 5L6-8 (Figure 4). In contrast, the 54-59 region exhibits markedly higher deuterium uptake either in WT or 5L6-8 (Figure 4). In addition, higher deuterium uptake (40-60%) was detected in the 205-214 peptide as compared with its inverted counterpart, the 47-59 peptide, both in WT and 5L6-8 (Figure 4). The present findings reveal that in the absence of Na^+ or Ca^{2+} , the OF and IF states share some common conformational patterns. For example, in both states the deuterium uptake of the ion-coordinating residues located on TM2B (S51 and E54) is lower than the deuterium uptake of the ion-coordinating residues located on TM7B (T209, E213, and D240). Notably, the observed low levels of deuterium uptake for TM2B represent either low water accessibility to the relevant domain and/or slow folding/unfolding kinetics of the local backbone entity. This represents a signature pattern of structure-dynamic preorganization within the ligand-free ion-binding pocket, which precedes (and largely predefines) the upcoming events of ion binding/occlusion and swapping of the OF/IF states.

Ca^{2+} - or Na^+ -induced conformational effects on WT and 5L6-8

For analyses of the Na^+ - or Ca^{2+} -bound forms of the WT and 5L6-8 proteins, 100 mM Na^+ (Figure 5) or 2 mM Ca^{2+} (Figure 6) were added to the samples, respectively and the deuterium uptake was

plotted as a function of time in Figures 5A (Na^+) and 6A (Ca^{2+}). In general, either Na^+ or Ca^{2+} binding results in overall reduced deuterium uptake in both the OF and IF states.

The ion-bound 5L6-8 (stabilized in the IF state) takes up more deuterium at specific regions as compared with the ion-bound WT (stabilized in the OF state). Notably, the region 40-46 (TM2A) maintains a similar deuterium uptake in the presence or absence of ligands. In contrast, the region 48-52 (TM2B), which harbors ion-coordinating residues (T50, S51), is protected by ligand binding, although this effect is more prominent for WT than for 5L6-8. Similarly, peptides 194-204 (TM7A), 205-214 (TM7B, encompassing ion coordinating residues A206, T209, S210, and E213), 215-230 (TM7C and the beginning of TM8A) and 238-245 (TM8B) are protected by ion binding and the effect is more marked for WT in comparison with 5L6-8 (Figures 4-6). In summary, Na^+ ligation in WT (but not in 5L6-8) via A47, T50, and S51 at the S_{int} site or Ca^{2+} ligation in WT (but not in 5L6-8) via T50, S51, and E54 at S_{Ca} can stabilize the backbone dynamics upon ion binding within and nearby the ion-binding site. In contrast to the regions protected by ion binding, region 204-205 (TM7A-TM7B hinge) exhibits high deuterium uptake in the presence of ligands. Region 231-237, representing TM8A, is largely unaffected by ligand binding.

Collectively, the effects of both ions are quite similar for a given protein but are characteristically different when comparing two proteins, stabilized in the OF (WT) or IF (5L6-8) state (Figures 5 and 6). This is consistent with MD simulations suggesting that the Na^+ and Ca^{2+} ions might induce similar conformational changes upon Na^+ or Ca^{2+} binding/occlusion in the WT protein (26). Even though Na^+ or Ca^{2+} modifies the backbone dynamics at specific segments within and nearby the ion-binding pocket, the overall conformational patterns of each protein (WT or 5L6) remain quite

similar in comparison with their own apo states (Figures 4-6). These data strongly support the notion that conformational patterns of apo proteins largely predefine the incremental effects of ion-binding/occlusion. The most striking finding is that either the Na^+ or Ca^{2+} binding results in conformational more stable (more rigid) species in the OF than in the IF state, thereby suggesting that the overall kinetics (including the ion bound/occluded states) of ion release is much slower on the extracellular than on the cytosolic side (Figures 4-6). This may represent a structure-dynamic basis for intrinsic asymmetry of bidirectional ion movements, detected by ion-flux assays in the vesicular preparations of membrane-bound NCX (23,25,28).

Diverse stabilities of the ion-occluded states at the cytosolic and extracellular vestibules

For a quantitative visualization of the local conformational changes induced by ion binding/occlusion in the OF and IF stabilized states, the differential HDX signals induced by Na^+ (Na^+ -apo) or Ca^{2+} (Ca^{2+} -apo) binding were calculated by subtracting the deuterium levels of the apo state from the ion-bound state (Figure 7). WT and 5L6-8 exhibit distinct changes in the local backbone dynamics upon ion binding, where the ΔHDX values vary from -30% to +10% in WT and from -15% to +5% in 5L6-8 (Figure 7). Thus, specific regions undergo conformational changes upon ion binding, whereas the conformational stability values at the respective sites are different in WT (stabilized in the OF state) and 5L6-8 (stabilized in the IF state). Namely, the binding of either Na^+ or Ca^{2+} to WT results in strong backbone rigidification of TM2B, whereas they have lesser effects on TM2A, TM2C, TM7AB, and TM8AB (Figure 7A). In contrast with WT, either Na^+ or Ca^{2+} binding to 5L6-8 results in less rigidification of TM2AB with no remarkable changes in the TM7AB and TM8AB backbone dynamics (Figure 7B).

For comparison between the Ca^{2+} and Na^+ induced effects, the deuterium levels of the Ca^{2+} -bound state were subtracted from the Na^+ -bound state (assigned as Na^+ - Ca^{2+}). In general, the observed effects of Na^+ and Ca^{2+} binding are quite similar in a given protein although some slight conformational differences can be distinguished between the Na^+ and Ca^{2+} bound species (Figure 7). Namely, TM7AB is similarly deuterated in Na^+ -bound and Ca^{2+} -bound WT except for the 204-205 region at the TM7A-TM7B hinge, which is slightly more dynamic in the Na^+ -bound state. The Na^+ -bound state is slightly more dynamic (more deuterated) than the Ca^{2+} -bound state in 5L6-8 throughout TM7AB (Figure 7A,B). However, the opposite is true for the symmetry-related TM2A region, which is similarly stabilized by both ions in 5L6-8, but not in WT. Although there are small (but detectable) differences between the Na^+ and Ca^{2+} -dependent HDX signals (the Ca^{2+} -bound states are little bit more stable than the Na^+ -bound states), the 3Na^+ - or Ca^{2+} -bound/occluded state is consistently more stable in the OF than in the IF state (Figures 5-7). Thus, the OF- and IF-occluded states differ in their stability no matter which ion (Ca^{2+} or Na^+) is bound to the protein. These structure-dynamic differences between the OF- and IF-occluded states may represent a mechanistic basis for physiologically relevant differences in the ion-release kinetics and apparent affinities (K_{ms}) of transported ions at the cytosolic and extracellular sides (23,25,28).

DISCUSSION

Despite huge differences in the ion-transport kinetics (turnover rates of the transport cycle), NCX variants share a functional asymmetry for bidirectional ion movements (23-28). At this end, it is unclear how this functional asymmetry is controlled (if at all) by swapping of the OF/IF states and if so, what are the relevant structure-dynamic determinants of asymmetry. The present work was

undertaken to analyze the structure-dynamic features of apo and ion-bound forms in the OF (WT) and IF (5L6-8) states of NCX_Mj with the goal of elucidating the underlying mechanisms of the ion-coupled OF/IF swapping.

Purified apo 5L6-8 preferentially adopts the IF orientation in solution.

High-resolution X-ray data of isolated NCX_Mj (14,26) and kinetic analyses of membrane-bound NCX_Mj (23,28,33) have established that the WT protein preferentially adopts the OF state. Although the kinetic analysis revealed that the membrane-bound 5L6-8 adopts the IF state, structural evidence was lacking (23,28). For this reason, it was essential to resolve this issue by using an independent experimental approach, related to the orientation of cytosolic and extracellular vestibules to the bulk face. For this purpose, the covalent labeling of structurally predefined single-cysteine mutants were tested in purified WT and 5L6-8 NCX_Mj by using the covalent fluorescent probe, TMRM maleimide (42,43). The positions of single-cysteine mutations were carefully designed according to the crystal structure of NCX_Mj and computer-aided modeling of IF NCX_Mj predicting that G42 (at extracellular vestibule) and G201 (at cytosolic vestibule) should be alternatively exposed to the bulk phase in the OF and IF states (Figure 2). Ion-flux assays confirmed that the used single-cysteine mutations do not alter the ion-transport activities in the vesicular preparations containing the overexpressed NCX_Mj (see Materials and Methods). The TMRM-reactivity of G201C and G42C demonstrated that in solution, the purified apo-forms of WT and 5L6-8 adopt the OF and IF orientations, respectively (Figure 2). This experimental validation is important for conclusive interpretation of HDX-MS data for the purified 5L6-8 protein (adopting the IF orientation), since the crystal structure of the IF state is unavailable.

Hallmark dynamic profiles provide a clue for ion-coupled alternating access

The striking finding is that in both apo proteins (WT and 5L6-8), the TM2B segment is much more constrained (less flexible) than the neighboring TM2C, TM7B and TM7C (Figures 4-7). These signature patterns of structure-dynamic preorganization involve key residues controlling the ion-transport activities [23,28]. These observations are especially interesting in perspective of structural evidence that the ion occlusion closes up a hydrophilic gap between P53 (TM2C) and P212 (TM7B), thereby yielding a hydrophobic patch (14-17,26). Crystal structures of NCX and similar proteins provided a clue that formation of hydrophobic patch upon ion occlusion may promote the sliding motion of the gating bundle (TM1/TM6) (15). The present HDX-MS data demonstrate that either in the Na⁺ or Ca²⁺ occluded state the hydrophobic patch is not entirely stable, since TM2C, TM7B and TM7C remain quite flexible either in the Na⁺ or Ca²⁺ occluded state (Figures 8). Thus, it is reasonable to propose that dynamic stability of the hydrophobic patch in the ion-occluded states is insufficient for the movement of the gating bundle. Thus, the ion occlusion may decrease the energy barrier for the movement of the gating bundle, but this may be not enough for accomplishing the alternating access.

Crystal structure of NCX-Mj depicts six oxygen ligation centers for Ca²⁺ coordination: two from the backbone carbonyls of T50 and T209 and four from the carboxyl groups of E54 and E213 (14,16). Notably, all these residues belong to the signature sequence of GTSLPE within the α_1 (aa 49-54) and α_2 (aa 208-214) repeats (14,26). Extended kinetic analyses of single-point mutations revealed that the side-chains of six residues (S51, E54, S77, E213, D240 and T209) are essential for ion-transport activities, thereby suggesting that these “catalytic” residues may stabilize the

Ca^{2+} -bound species in the transition state (27,28). In this context, we posit that in the transition state the Ca^{2+} -bound species stabilize the hydrophobic patch between TM2C (P53) and TM7C (P212), which allows the relocation (sliding) of the gating bundle (TM1/TM6) toward the OF/IF swapping (Figure 9A). The rationale behind is that the mobile segments (TM7B, TM7C, TM2C and TM8A) become rigidified in front of "ever-rigid" TM2B in the ion-bound transition state that admits the movement of the gating bundle (dashed TM1/TM6 cluster in Figures 8 and 9A). This proposal underscores the basis of ion-coupled alternating access in NCX and similar proteins, since only the transition state (and not the occluded state) can change the status of the gating bundle relocation, toward accomplishing the alternating access. This proposal may serve as a good platform for mechanism-based MD simulations, which can conclusively evaluate rational aspects of the present working hypothesis and may provide additional mechanistic insights as well.

Dynamic differences between the OF and IF states in the apo forms

Despite structure-dynamic similarities between the OF and IF states described above, there are striking differences in the local backbone dynamics assigned to specific regions at the cytosolic and extracellular sides. Namely, TM2A and TM8A are more flexible in apo-5L6-8 than in apo WT, whereas the opposite is true for TM7A (which is pseudo-symmetrical to TM2A) (Figure 4). Moreover, the OF state (apo WT) possesses higher water accessibility at the extracellular than at the cytosolic entry, whereas the opposite is true for the IF state (apo 5L6-8) (Figure 4). Thus, pseudo-symmetry-related structural entities at the cytosolic and extracellular entries exhibit reciprocal levels of deuterium uptake in the apo-IF and apo-OF states, thereby representing hallmark differences in the structure-dynamic preorganization of the

OF and IF states prior to ion binding/occlusion. That is, our results corroborate that apo-NCX does not alternate between the OF/IF state; otherwise, one may expect a similar (if not identical) HDX uptake for the OF and IF-stabilized proteins (Figure 8). Thus, HDX patterns of apo WT and 5L6-8 are in agreement with a general dogma suggesting that the ligand binding to the antiporter is obligatory for effective swapping the OF/IF states (2-7). The mechanistic significance of this is that the asymmetric preorganization of ligand-free ion-binding pocket preconditions the ion binding effects at specific locations, which actually predefine the strength and specificity of ion binding. Thus, structure-dynamic preorganization of NCX underscores the importance of apo-protein conformational state.

Na^+ or Ca^{2+} binding differentially rigidifies (stabilizes) the OF and IF states.

The binding of either Na^+ (Figure 5) or Ca^{2+} (Figure 6) induces moderate (but specific) changes in the local backbone dynamics, either in WT or 5L6-8, where the ion-dependent differential HDX signals are comparable for both ions in a given protein (Figure 7). Nevertheless, the Na^+ - and Ca^{2+} -bound forms exhibit reliable differences in the differential HDX signals, revealing that Na^+ -bound species are slightly more flexible than are the Ca^{2+} -bound species. Namely, the 204-205 region (TM7A-TM7B hinge) exhibits differences between the OF- and IF-occluded states: Na^+ (but not Ca^{2+}) binding destabilizes this region in WT, whereas either Na^+ or Ca^{2+} stabilizes this region in 5L6-8 (Figure 7). These data are especially interesting in the context of structural evidence demonstrating that backbone bending at the interface of TM7A and TM7B (203-205) accompanies 3Na^+ occlusion in the OF state (26). According to the HDX-MS data, the bending of TM7 upon 3Na^+ binding may have an additional important outcome in

forming a hydrophobic interface with the C-terminus of TM6. Moreover, hydrophobic interactions between TM6 and TM7 (involving L204) are highly probable without Na^+ , which is consistent with higher solvent exposure (higher deuterium uptake) observed upon Na^+ binding. These "small" conformational changes could be related to "pore-narrowing" events preceding the sliding of the TM1/TM6 gating bundle toward OF/IF swapping (15). Although the present data cannot either conform or reject the "pore-narrowing" hypothesis, compiling data are consistent with a notion that the IF and OF states retain highly asymmetric dynamic patterns upon ion binding/occlusion, where the ion binding has relatively small effects on backbone rigidity (Figure 8). In line with general concepts (44-46) the ligand binding may cause small changes in the local backbone dynamics (e.g., a partial stabilization of the ion-binding pocket upon the ion occlusion) toward more "global" conformational changes that occur in the continuation (e.g., the sliding of the TM1/TM6 cluster)(Figures 9A).

Distinctly stabilized occluded states may control ion-release dynamics at opposite sides

The general observation is that the ion-binding regions are more stable (rigid) in WT than in 5L6-8, when comparing these two proteins either in the Ca^{2+} - or Na^+ -bound form (Figures 6 and 7). Thus, a more stable conformational patterns of ion-bound species in the OF than in the IF state (Figure 8) can limit ion binding/release kinetics and thus, the apparent affinity (K_m) at opposite sides of the membrane (Figure 9B). This may represent a principal mechanism for generating intrinsic asymmetry in the antiporter system, where conformational preorganization in the apo state diversifies the strength and duration of ion-occlusion states at the opposite sides of the membrane. This scenario underscores the role of conformational dynamics

possessed by the apo protein, which actually predefines the extent of intrinsic asymmetry, even though the binding of Na^+ or Ca^{2+} secondarily modifies the preexisting conformational patterns of the apo-protein (Figures 5-7). Consistent with this, the Na^+ -dependent interaction between TM6 and TM7 is clearly supported by HDX-MS (Figures 4-7). The significance of these interactions stem from the fact that the sliding trajectory of the gating bundle (TM1/TM6 cluster) against the rigid eight-helix core (TM2-TM5 and TM7-TM10) may represent a major conformational change that occurs in the Ca^{2+} /cation exchanger superfamily (14-17). Conceptually, it is essential to mention that the transition state (and not the occluded state) must be induced by the movement of the TM1/TM6 cluster toward the OF/IF swapping. Thus, it is expected that the TM1/TM6 cluster does not move after the occlusion of 3Na^+ (26). The present data demonstrate that the OF- and IF-occluded states significantly differ in their conformational stability (Figures 4-6). This puts forward the two-occluded/one-transition state model, which is essential for completion of the ion-exchange cycle (Figures 9B). This model fundamentally differs from commonly used models describing a "single" occluded state, placed between the OF and IF ground states.

Conclusions

The present work has identified conformational differences assigned to the apo- and ion-bound forms of NCX_Mj, stabilized in the OF and IF states. The central findings are that the apo proteins exhibit different dynamic features and the ion-bound species adopting the OF orientation are more stable (more rigid) than the ion-bound species in the IF state (Figure 8). Although the Na^+ or Ca^{2+} binding moderately (but specifically) modifies the backbone dynamics, the conformational differences observed for ion-bound species in the OF and IF states are largely predefined by signature

landscapes exemplified in the apo-OF and apo-IF protein structure (Figure 8). Since the dynamic features of ion-bound species in the OF- and IF-occluded states are encoded by the apo protein's structure, the mechanisms described here might also be relevant for similar proteins belonging to the Ca^{2+} /cation exchanger superfamily. In light of the present findings, it is reasonable to assume that structure-dynamic determinants, limiting the stability (rigidity) of ion-occluded species in the OF and IF states, can control the ion-release kinetics of occluded ions at the cytosolic and extracellular domains. These dynamic features may govern not only the turnover rates of transport cycle, but also the apparent affinities (K_m) of transported ions at opposite sides of the membrane. This may have physiological relevance since NCX-mediated cytosolic Ca^{2+} -extrusion rates vary over a four-order magnitude in different cells, where their values must precisely match dynamic swings in $[\text{Ca}^{2+}]_i$ in a given cell type.

MATERIALS AND METHODS

DNA construct preparation

DNA encoding the WT NCX_Mj was amplified by PCR from a *Methanocaldococcus jannaschii* cDNA library (DSMZ) and ligated between the NcoI and BamHI restriction sites of a pET-28a plasmid (23,27,28). Mutations were introduced according to the established procedures of QuickChange mutagenesis (Stratagene) and each mutation was confirmed by sequence analysis as outlined before (23,28).

Protein purification

NCX_Mj was overexpressed and purified as previously established (14,23,28). Briefly, membranes were isolated from the cell lysate by ultracentrifugation and after membrane protein extraction with 20 mM DDM (n-Dodecyl β -D-maltoside), the supernatant was loaded onto a Co^{2+} affinity column (TALON) and protein was eluted with 300 mM imidazole and 4mM DDM. Protein

was then desalted to eliminate imidazole with a buffer containing 4 mM DDM and then digested overnight with TEV protease. Following a second passage through the Co^{2+} column (with a buffer containing 2 mM DDM) to eliminate the His-tag and TEV protease, the protein was purified on Superdex-200 pre-equilibrated with 0.5 mM DDM buffer. Concentrated (1-5 mg/ml) preparations of purified proteins (> 95% purity, as judged by SDS-PAGE), were stored at -80°C in buffer containing 0.5 mM DDM.

Site-directed labeling of single-cysteine mutants by TMRM in purified WT and 5L6-8 NCX_Mj

Stock solutions of 200-500 μM TMRM (tetramethylrhodamine-5-maleimide) were prepared by dissolving TMRM in DMSO. The final concentrations of the TMRM stock solutions were determined by measuring their absorbance in methanol at 541 nm with an extinction coefficient of $95,000 \text{ cm}^{-1} \text{ M}^{-1}$ (42,43). Purified preparations of single-cysteine-mutated WT or 5L6 NCX_Mj (0.2-0.3 mg protein/ml in 100 mM KHPO_3 buffer, pH 7.1) were incubated with 1 μM TMRM at 4°C for 0-30 minutes. Then 30-40 μl aliquots were removed from the reaction mixture and covalent labeling was terminated at the indicated times by adding 500 mM DTT to a final concentration of 10 mM DTT. An equal volume of SDS-PAGE loading buffer was added to each quenched sample and then the samples were subjected to SDS-PAGE analysis. The gels were imaged using a Fusion FX7 Spectra instrument (Vilber LourmatTM) equipped with "Fusion-Capture Advance" software. The rhodamine images were captured by adjusting the excitation and emission wavelengths to 540 nm and 595 nm, respectively. The TMRM signals were quantified by measuring the density of each band with Fusion-Capture Advance software (Vilber LourmatTM). The first-order rate constants for TMRM maleimidelabeling were derived by

plotting the TMRM-band signals vs time (for each gel) and the experimental points were fit using GraFit 7.1 software (Erithacus Software, Ltd.) according to the equation $Y = \text{limit} \times (1 - e^{-kt})$.

Hydrogen/Deuterium exchange Mass Spectrometry (HDX MS)

HDX MS experiments were fully automated using a PAL autosampler (CTC Analytics). This controlled the start of the exchange and quench reactions, the proteolysis temperature (4°C), the injection of the deuterated peptides, the management of the injection and washing valves, and it triggered the acquisition of the mass spectrometer and HPLC pumps. A Peltier-cooled box (4°C) contained two Rheodyne-automated valves (6-port for injection and 10-port for washing), a desalting cartridge (peptide Opti-Trap Micro from Optimize Technologies), and a HPLC column (Jupiter 4 μ m Proteo 90Å, 50x1 mm, Phenomenex). HDX MS reactions were carried out using different forms of WT or 5L6-8 (either in the apo form or in the presence of Na⁺ or Ca²⁺ ions) at a protein concentration of 40 μ M. Deuteration was initiated by a 5-fold dilution of the protein samples (10 μ L) with the same buffer in D₂O (40 μ L). The proteins were deuterated for 15 s, 120 s, or 1200 s at 4°C. Back-exchange quench and digestion were performed using 50 μ L of a porcine pepsin (Sigma) solution at 0.23 mg/mL in 100 mM glycine-HCl, pH 2.5 at 4°C for 1200 s. The peptides were desalted for 6 min using a HPLC pump (Agilent Technologies) with 0.03% TFA in water at a flow rate of 100 μ L/min. The peptides were then separated using HPLC pump (Agilent Technologies) at 50 μ L/min for 6 min with a 15-50% gradient of Buffer B (Buffer A: TFA 0.03 % in water; Buffer B: acetonitrile 90%, TFA 0.03% in water), followed by 9 min at 50% B and 1 min at 100% B. The peptide masses were measured using an electrospray-TOF mass spectrometer (Agilent 6210) in the 300-1300 m/z range. Each deuteration experiment was

replicated in triplicate. Mass Hunter (Agilent Technologies) software was used for data acquisition (28,46). HD Examiner software (Sierra Analytics) was used for HDX MS data processing (28). Peptides were identified as described previously (28). The identified peptides were plotted against the protein sequence using a web-based software package, MSTools, to visualize the sequence coverage (46).

⁴⁵Ca²⁺-uptake assay in *E. coli*-derived vesicles – *E. coli*-derived cell-membrane vesicles, containing overexpressed WT-G42C, WT-G201C, 5L6-8-G42C and 5L6-G201C were obtained as described for WT-NCX_Mj at stored at -80°C until use (23,27,28). The initial rates ($t = 5$ -10 seconds) of the Na⁺/Ca²⁺ and Ca²⁺/Ca²⁺ exchange reactions were assayed by measuring ⁴⁵Ca²⁺-uptake in the *E. coli*-derived vesicles as established for the standard assay conditions (23,27,28). Briefly, Na⁺ or Ca²⁺-loaded vesicles were rapidly diluted (25-50-fold) in an assay medium containing 20 mM MOPS/Tris, pH 6.5, 100 mM KCl, and varying concentrations (5-2000 μ M) of ⁴⁵CaCl₂ (at 35°C). The ⁴⁵Ca²⁺-uptake was quenched by rapid addition of cold buffer containing 10 mM EGTA and quenched samples were filtrated on GF/C filters, as outlined before (23,28,47). The K_m and V_{max} values were measured for each mutant in at least three independent experiments and the data were analyzed with GraFit 7.1 software (Erithacus Software, Ltd.) (23,28,27). The observed K_m and V_{max} values of WT-G42C, WT-G201C, 5L6-8-G42C and 5L6-G201C were ranging in the range of 80-100% as compared with WT-NCX_Mj, thereby suggesting that the single-cysteine mutations have a negligible (if any) effect on the ion-transport activities.

Computer-aided modeling

Computer-aided modeling of the inward-facing conformation was generated by exploiting the intrinsic symmetry of NCX-Mj (14,23,28). MODELLER (48) was

used to generate the models. The structure of each half of the protein was generated using the homology to the opposite symmetric part and sequence alignments

of NCX-Mj's helical segments TM1-3 to TM6-8 and TM4-5 to TM 9-10, along with the exact opposite order alignments.

Acknowledgments

This work was funded by the Israel Science Foundation Grant #825/14 to DK. The support of the Fields Estate Foundation to DK is highly appreciated. PM acknowledges support from EU/MEYS (LQ1604 and CZ.1.05/1.1.00/02.0109).

Competing interests

The authors declare no competing interests.

Author contributions

M.G., L.A., E.F., P.M., and D.K. designed the experiments. L.A., M.G., P.M., L.vD., B.R., and R.H. conducted the experiments. M.G., L.A., R.H., E.F., P.M., and D.K. analyzed and interpreted the experimental data. M.G. and D.K. wrote the manuscript.

REFERENCES

1. Jardetzky, O. (1966). Simple allosteric model for membrane pumps. *Nature* **211**, 969-970.
2. Kaback, H. R., Smirnova, I., Kasho, V., Nie, Y., & Zhou, Y. (2011). The alternating access transport mechanism in LacY. *J. Membr. Biol.* **239**, 85-93.
3. Keller, R., Ziegler, C., & Schneider, D. (2014). When two turn into one: evolution of membrane transporters from half modules. *Biol. Chem.* **395**, 1379-1388.
4. Forrest, L. R., Krämer, R., & Ziegler, C. (2011). The structural basis of secondary active transport mechanisms. *Bioch. Biophys. Acta.* **1807**, 167-188.
5. Deng, D., & Yan, N. (2016). GLUT, SGLT, and SWEET: Structural and mechanistic investigations of the glucose transporters. *Protein Sci.* **25**, 546-558.
6. Drew, D., & Boudker, O. (2016). Shared molecular mechanisms of membrane transporters. *Ann. Rev. Biochem.* **85**, 543-572.
7. Giladi, M., Tal, I., & Khananshvil, D. (2016). Structural features of ion transport and allosteric regulation in sodium-calcium exchanger (NCX) proteins. *Front. Physiol.* **7**, 30, doi:10.3389/fphys.2016.00030.
8. Carafoli, E. (1987) Intracellular calcium homeostasis. *Ann. Rev. Biochem.* **56**, 395-433.
9. Philipson, K. D. & Nicoll, D. A. (2000). Sodium-calcium exchange: a molecular perspective. *Ann. Rev. Physiol.* **62**, 111-133.
10. Khananshvil, D. (2013). The SLC8 gene family of sodium-calcium exchangers (NCX)-structure, function, and regulation in health and disease. *Mol. Aspects Med.* **34**, 220-235.
11. Khananshvil, D. (2014). Sodium-calcium exchangers (NCX): Molecular hallmarks underlying the tissue-specific and systemic functions. *Plügers Arch.* **466**, 43-60.
12. Lytton, J. (2007) Na⁺/Ca²⁺ exchangers: three mammalian gene families control Ca²⁺-transport. *Biochem. J.* **406**, 365-382.
13. On, C., Marshall, C. R., Chen, N., Moyes, C. D., & Tibbits, G. F. (2008). Gene structure evolution of the Na⁺-Ca²⁺ exchanger (NCX) family. *BMC Evolutionary Biology.* **8**, 127-142.
14. Liao, J., Li, H., Zeng, W., Sauer, D. B., Belmares, R., & Jiang, Y. (2012). Structural insight into the ion-exchange mechanism of the sodium/calcium exchanger. *Science* **335**, 686-690.
15. Nishizawa, T., Kita, S., Maturana, A. D., Furuya, N., Hirata, K., Kasuya, G., Ogasawara, S., Dohmae, N., Iwamoto, T., Ishitani, R., & Nureki, O. (2013). Structural basis for the counter-transport mechanism of a H⁺/Ca²⁺ exchanger. *Science* **341**, 168-172.

16. Waight, A. B., Pedersen, B. P., Schlessinger, A., Bonomi, M., Chau, B. H., Roe-Zurz, Z., Risenmay, A. J., Sali, A., & Stroud, R. M. (2013). Structural basis for alternating access of a eukaryotic calcium/proton exchanger. *Nature*. **499**, 107–110.
17. Wu, M., Tonga, S., Waltersperger, S., Diederichs, K., Wang, M., & Zheng, L. (2013). Crystal structure of $\text{Ca}^{2+}/\text{H}^{+}$ antiporter protein YfkE reveals the mechanisms of Ca^{2+} efflux and its pH regulation. *Proc. Natl. Acad. Sci. USA*. **110**, 11367–11372.
18. Schnetkamp, P. P. (2013). The SLC24 gene family of $\text{Na}^{+}/\text{Ca}^{2+}\text{-K}^{+}$ exchangers: from sight and smell to memory consolidation and skin pigmentation. *Mol. Aspects Med.* **34**:455–464.
19. Reeves, J. P., & Hale, C. C. (1984). The stoichiometry of the cardiac sodium-calcium exchange system. *J. Biol. Chem.* **259**, 7733–7739.
20. Bers, D. M., & Ginsburg, K. S. (2007) $\text{Na}:\text{Ca}$ stoichiometry and cytosolic Ca -dependent activation of NCX in intact cardiomyocytes. *Ann. N.Y. Acad. Sci.* **1099**, 326–338.
21. Khananshvil, D. (1990). Distinction between the two basic mechanisms of cation transport in the cardiac $\text{Na}^{+}\text{-Ca}^{2+}$ exchange system. *Biochemistry*. **29**, 2437–2442.
22. Niggli, E., & Lederer, W. J. (1991). Molecular operations of the sodium-calcium exchanger revealed by conformational currents. *Nature* **349**, 621–624.
23. Almagor, L., Giladi, M., van Dijk, L., Buki, T., Hiller, R., & Khananshvil, D. (2014). Functional asymmetry of bidirectional Ca^{2+} -movements in an archaeal sodium-calcium exchanger (NCX_Mj). *Cell Calcium* **56**, 276–284.
24. Baazov, D., Wang, X., & Khananshvil, D. (1999) Time-resolved monitoring of electrogenic $\text{Na}^{+}\text{-Ca}^{2+}$ exchange in the isolated cardiac sarcolemma vesicles by using a rapid-response fluorescent probe. *Biochemistry* **38**, 1435–1445.
25. Khananshvil, D., Weil-Maslansky, E., & Baazov, D. (1996). Kinetics and mechanism: modulation of ion transport in the cardiac sarcolemma sodium-calcium exchanger by protons, monovalent ions, and temperature. *Ann. N. Y. Acad. Sci.* **779**: 217–235.
26. Liao, J., Marinelli, F., Lee, C., Huang, Y., Faraldo-Gómez, J. D., & Jiang, Y. (2016). Mechanism of extracellular ion exchange and binding-site occlusion in a sodium/calcium exchanger. *Nat. Struct. Mol. Biol.* **23**, 590–599.
27. Marinelli, F., Almagor, L., Hiller, R., Giladi, M., Khananshvil, D., & Faraldo-Gómez J. D. (2014). Sodium recognition by the $\text{Na}^{+}/\text{Ca}^{2+}$ exchanger in the outward-facing conformation. *Proc. Natl. Acad. Sci. USA*. **111**, E5354–E5362.
28. Giladi, M., Almagor, L., van Dijk, L., Hiller, R., Man, P., Forest, E., & Khananshvil, D. (2016). Asymmetric preorganization of inverted pair residues in the sodium-calcium exchanger. *Sci. Rep.* **6**, 20753.
29. DiPolo, R., & Beaugé, L. (2006). Sodium/calcium exchanger: Influence of metabolic regulation on ion carrier interactions. *Physiol. Rev* **86**, 155–203.
30. Forrest, L. R. (2013). (Pseudo-) symmetrical transport. *Science* **339**, 399–341.
31. Forrest L. R. (2015). Structural symmetry in membrane proteins. *Ann. Rev. Biophys.* **44**, 311–337.
32. Stein, W. D. (1986). In: *Transport and Diffusion across Cell Membranes*, pp. 55–120. Academic Press, New York.
33. Giladi, M., Shor, R., Lisnyansky, M., & Khananshvil, D. (2016). Structure-functional basis of ion transport in sodium-calcium exchanger (NCX) proteins. *Int. J. Mol. Sci.* **17**(11). pii: E1949. DOI:10.3390/ijms17111949.
34. Bai, Y., Englander, J. J., Mayne, L., Milne, J. S., & Englander, S. W. (1995). Thermodynamic parameters from hydrogen exchange measurements. *Meth. Enzymol.* **259**, 344–356.
35. Englander, J. J., Del Mar, C., Li, W., Englander, S. W., Kim, J. S., Stranz, D. D., Hamuro, Y., & Woods, V. L. Jr. (2003). Protein structure change studied by hydrogen-deuterium exchange, functional labeling, and mass spectrometry. *Proc. Natl. Acad. Sci. USA*. **100**, 7057–7062.

36. Konermann, L., Pan, J., & Liu, Y. H. (2011). Hydrogen exchange mass spectrometry for studying protein structure and dynamics. *Chem. Soc. Rev.* **40**, 1224-1234.
37. Chalmers, M. J., Busby, S. A, Pascal, B. D, West, G. M., & Griffin, P. R. (2011). Differential hydrogen/deuterium exchange mass spectrometry analysis of protein-ligand interactions. *Exp. Rev. Proteom.* **8**, 43-59.
38. Demmers, J. A., Haverkamp, J., Heck, A. J, Koeppe, R. E. II., & Killian, J. A. (2000). Electrospray ionization mass spectrometry as a tool to analyze hydrogen/deuterium exchange kinetics of transmembrane peptides in lipid bilayers. *Proc. Natl. Acad. Sci. USA* **97**, 3189-3194.
39. Giladi, M., Lee, S.Y., Ariely, Y., Teldan, Y., Granit, R., Strulovich, R., Haitin, Y., Chung K.Y., & Khananshvili, D. (2017) Structure-based dynamic arrays in regulatory domains of sodium-calcium exchanger (NCX) isoforms. *Sci. Rep.* 7(1):993. doi: 10.1038/s41598-017-01102-x.
40. Giladi, M., Lee, S. Y., Hiller, R., Chung, K. Y., & Khananshvili, D. (2015). Structure-dynamic determinants governing a mode of regulatory response and propagation of allosteric signal in splice variants of Na⁺/Ca²⁺ exchange (NCX) proteins. *Biochem. J.* **465**, 489–501.
41. Lee, S. Y., Giladi, M., Bohbot, H., Hiller, R., Chung, K. Y., & Khananshvili D. (2016). Structure-dynamic basis of splicing dependent regulation in tissue-specific variants of the sodium-calcium exchanger (NCX1). *FASEB J.* **30**, 1356-1366.
42. Nie, Y., Ermolova, N., & Kaback, H. R. (2007). Site-directed alkylation of LacY: effect of the proton electrochemical gradient. *J. Mol. Biol.* **374**, 356-364. DOI:10.1016/j.jmb.2007.09.006.
43. Jiang, X., Nie, Y., & Kaback, H. R. (2011). Site-directed alkylation studies with LacY provide evidence for the alternating access model of transport. *Biochemistry* **50**, 1634-40. doi: 10.1021/bi101988s.
44. Tsai, C. J., Ma, B., & Nussinov, R. (1999). Folding and binding cascades: shifts in energy landscapes. *Proc. Natl. Acad. Sci. USA.* **96**, 9970-9972.
45. Gifford, J.L., Walsh, M.P., & Vogel, H.J. (2007). Structures and metal-ion-binding properties of the Ca²⁺-binding helix-loop-helix EF-hand motifs. *Biochem J.* **405**, 199-221.
46. Tsai, C.J., del Sol, A., & Nussinov R. (2008) Allostery: absence of a change in shape does not imply that allostery is not at play. *J Mol Biol* **378**, 1-11. doi: 10.1016/j.jmb.2008.02.034
46. Kavan, D., & Man, P. (2011). MStools - Web based application for visualization and presentation of HDX-MS data. *Int. J. Mass. Spectrom.* **302**, 53-58.
47. Refaeli, B., Giladi, M., Hiller, R., & Khananshvili, D. (2016). Structure-based engineering of lithium transporting capacity in the archaeal sodium–calcium exchanger (NCX_Mj). *Biochemistry* **55**, 1673–1676.
48. Marti-Renom, M. A., Stuart, A., Fiser, A., Sánchez, R., Melo, F., & Sali, A. (2000). Comparative protein structure modeling of genes and genomes. *Ann. Rev. Biophys. Biomol. Struct.* **29**, 291-325.

FIGURE LEGENDS

Figure 1. Structure of NCX_Mj. Crystal structures of NCX_Mj in (A) apo (PDB 5HXH), (B) occluded, 3Na⁺-bound (PDB 5HXE), and (C) semi-open, Ca²⁺-bound (PDB 5HXR) conformations in cartoon representation. Helices 1-5 (TM1-5) are orange and helices 6-10 (TM6-10) are purple. Purple and green spheres represent Na⁺ and Ca²⁺ ions, respectively. (D) 3Na⁺ ion coordination. Ion-coordinating residues are represented as sticks. The red sphere represents a water molecule. (E) Ca²⁺ binding site. Ion coordinating residues are represented as sticks. (F) Schematic representation of the ligand-induced conformational transitions in the outward-facing (OF) orientation. Green and red spheres represent Na⁺ and Ca²⁺ ions, respectively. The gating bundle (TM1 and TM6) is represented by a dashed line.

Figure 2. TMRM maleimide reactivity of G201C and G42C mutants in the WT and 5L6-8 proteins. Purified WT-G201C, WT-G42, 5L6-8-G201C, and 5L6-8-G42C proteins (0.1-0.3 mg/ml) were incubated with 1μM TMRM maleimide at 4 °C for 0-30 minutes as described in Materials and Methods. At the indicated times, the reaction of TMRM labeling was terminated by DTT and the quenched samples were subjected to SDS-PAGE. The TMRM-labeled bands corresponding to each cysteine-mutant protein were imaged and measured quantitatively as described in Materials and Methods. (A) TMRM maleimide reactivity of WT-G201C and WT-G42C. Experimental points were fitted to calculated curves (see Materials and Methods) representing the first-order rate constants of $0.25 \pm 0.04 \text{ s}^{-1}$ and $0.02 \pm 0.01 \text{ s}^{-1}$ for WT-G201C (red circles) and WT-G42C (blue triangles), respectively. The crystal structure of the outward-facing (OF) orientation of NCX_Mj is presented as outlined in Figure 1. (B) TMRM maleimide reactivity of 5L6-8-G201C and 5L6-8-G42C. Experimental points of proteins labeled with TMRM collected and plotted as described in the legend of panel A. The fitted curves represent the first-order rate constants of $0.28 \pm 0.06 \text{ s}^{-1}$ and $0.057 \pm 0.010 \text{ s}^{-1}$ for WT-G42C (blue triangles) and WT-G201C (red circles), respectively. The inward-facing (IF) image of NCX_Mj was computed as described in Materials and Methods.

Figure 3. HDX-MS sequence coverage of NCX_Mj. The transmembrane helices are shown above the sequence. Peptic peptides are displayed as black bars below the sequence. The regions 41-59 (TM2) and 195-264 (from TM7 to the beginning of TM9) were covered by three and eight peptides, respectively. A small portion of TM9 was also found (peptide 259-264). Four couples of overlapping peptides (possessing a common extremity) enabled us to locally increase the resolution, providing information about small segments (2-7 amino acids).

Figure 4. HDX-MS analysis of NCX_Mj in the apo state. (A) Deuterium uptake plots in the apo state for the indicated regions in the WT protein (black) and 5L6-8 mutant (red). Data are presented as the mean \pm SD (n=3). The heat map for the (B) WT protein and the (C) 5L6-8 mutant in the apo state at 15, 120, and 1,200 sec is overlaid on the crystal structure of apo NCX_Mj (PDB 5HXH) and its modelled inward-facing state. The color key indicates the HDX level. The numberings indicate deuterium uptake regions (not taking into account the N-terminus amino acids of peptides without amide hydrogens).

Figure 5. HDX-MS analysis of NCX_Mj in the Na⁺-bound state. (A) Deuterium uptake plots in the Na⁺-bound state for the indicated regions in the WT protein (black) and 5L6-8 mutant (red). Data are presented as the mean \pm SD (n=3). The heat map for the (B) WT protein and the (C) 5L6-8 mutant in the Na⁺-bound state at 15, 120, and 1,200 sec is overlaid

on the crystal structure of 3Na⁺-bound NCX_Mj (PDB 5HXE) and its modelled inward-facing state. The color key indicates the HDX level. The numberings indicate deuterium uptake regions (not taking into account the N-terminus amino acids of peptides without amide hydrogens).

Figure 6. HDX-MS analysis of NCX_Mj in the Ca²⁺-bound state. (A) Deuterium uptake plots in the Ca²⁺-bound state for the indicated regions in the WT protein (black) and the 5L6-8 mutant (red). Data are presented as the mean±SD (n=3). The heat map for the (B) WT protein and the (C) 5L6-8 mutant in the Na⁺-bound state at 15, 120, and 1,200 sec is overlaid on the crystal structure of Ca²⁺-bound NCX_Mj (PDB 5HXR) and its modelled inward-facing state. The color key indicates the HDX level. The numberings indicate deuterium uptake regions (not taking into account the N-terminus amino acids of peptides without amide hydrogens).

Figure 7. Effect of ligand binding on NCX_Mj dynamics. The difference between the HDX profile of the Na⁺-bound and apo forms (Na⁺-apo), Ca²⁺-bound and apo forms (Ca²⁺-apo), and Na⁺-bound and Ca²⁺-bound forms (Na⁺-Ca²⁺) of NCX_Mj at 1200 sec are overlaid on the crystal structure of NCX_Mj for the WT protein (A) and on the modelled inward-facing state for the 5L6-8 mutant (B). The color key indicates the difference in the percentage of deuterium incorporation between the indicated forms.

Figure 8. Observed backbone dynamics of apo, Ca²⁺- and Na⁺-bound species in the OF and IF states. Experimentally observed HDX signals (at 1200sec) were collected and plotted for WT (OF) and 5L6 (IF) proteins in the apo- Ca²⁺- and Na⁺-bound states as described in the legends of Figures 4-8. The color key indicates the difference in the percentage of deuterium incorporation between the indicated forms as described in Figures 4-6.

Figure 9. Schematic presentation of putative mechanisms underlying the ion-coupled alternating access in NCX_Mj. Panel A describes the proposed mechanism of ion-coupled alternative access for Ca²⁺-bound OF/IF swapping and panel B depicts differential stability of Na⁺- and Ca²⁺-occluded species in the OF- and IF states. (A) **Proposed mechanism of "one transition/two occluded state" mechanism for bound Ca²⁺.** In the Ca²⁺ occluded state the hydrophilic gap between the TM2C (P53) and TM7B (P212) segments is closed up yielding a hydrophobic patch (14,15,26). HDX-MS data reveal that TM2C, TM7B, TM7C and TM8A presiding the hydrophobic patch remain quite flexible upon ion occlusion (Figures 4-7). The stability of the hydrophobic patch can be enhanced by interaction of "catalytic" residues (E54, E213, D240, S51, S77 and T209) with Ca²⁺ in the transition state, where TM2C, TM7B, TM7C and TM8A become rigidified toward ever-rigid TM2B. The rationale behind is that the rigidified hydrophobic patch can stipulate the sliding of the gating bundle toward the OF/IF swapping (the dashed TM1/TM6 cluster in the transition state). The dotted cycle represents a putative position of Ca²⁺ in the transition state, which presumably differs from the Ca²⁺ position in the occluded state. (B) **Differential stability of ion-bound species in the OF- and IF occluded states.** The Na⁺/Ca²⁺ exchange cycle is described as a separate translocation of 1Ca²⁺ and 3Na⁺ ions. HDX-MS data reveal that the occlusion of either ion is more stable in the OF than in the IF state. The observed differences in the OF and IF conformational stability may account for differences in the ion-release dynamics and apparent affinity (K_m) at the extracellular and cytosolic sides. Thus, structurally encoded dynamic features of protein may predefine bidirectional asymmetry of the antiporter system, as can be detected in the ion-flux assays of intact (membrane-bound) NCX preparations. Green and red spheres represent the Na⁺ and Ca²⁺ ions, respectively and

the gating bundle (the TM1/TM6 cluster) is represented as a dashed line. The present proposal is consistent with "the one-transition/two-occluded state" model (see panel A), where the movement of the gating bundle is driven by the transition state and not by occlusion.

Table 1. Peptides and regions used for HDX-MS analysis.

Peptides	Regions	Region Positions
40-46	41-46	TM2
47-59	48-52	TM2
53-59	54-59	TM2
194-204	195-204	6L7, TM7
203-214	204-205	TM7
205-214	206-214	TM7
215-230	216-230	TM7-TM8
215-237	231-237	TM8
238-245	238-245	TM8
238-250	246-250	TM8
259-264	260-264	TM9

Peptides indicate the detected proteolytic digestion products of NCX_Mj. The regions do not take into account the N-terminus amino acids of each peptide (e.g., peptide 40-46 vs. region 41-46) nor are they calculated from the difference between two overlapping peptides (e.g., region 48-52 calculated from the overlapping peptides 47-59 and 53-59).

Figure 1

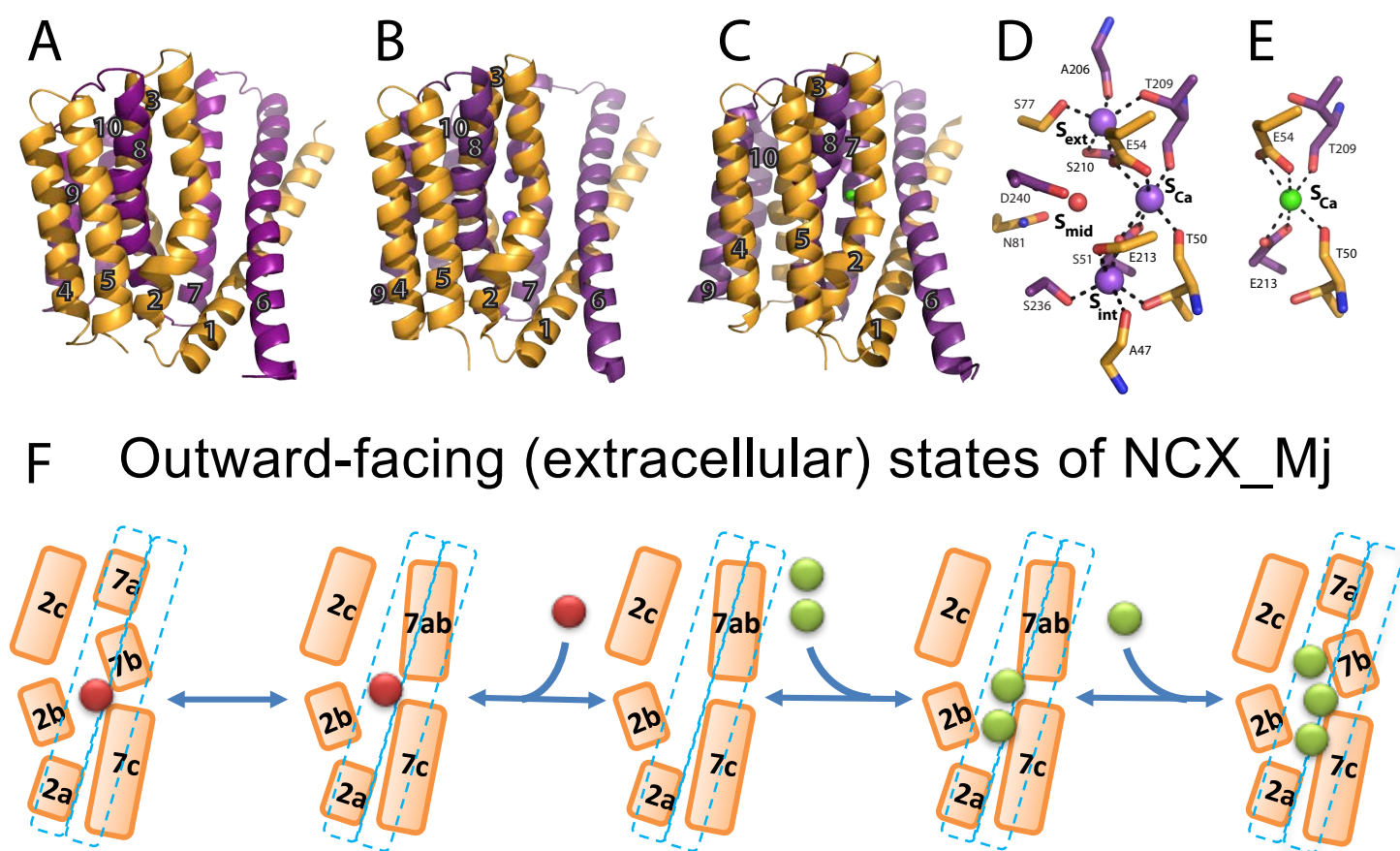


Figure 2

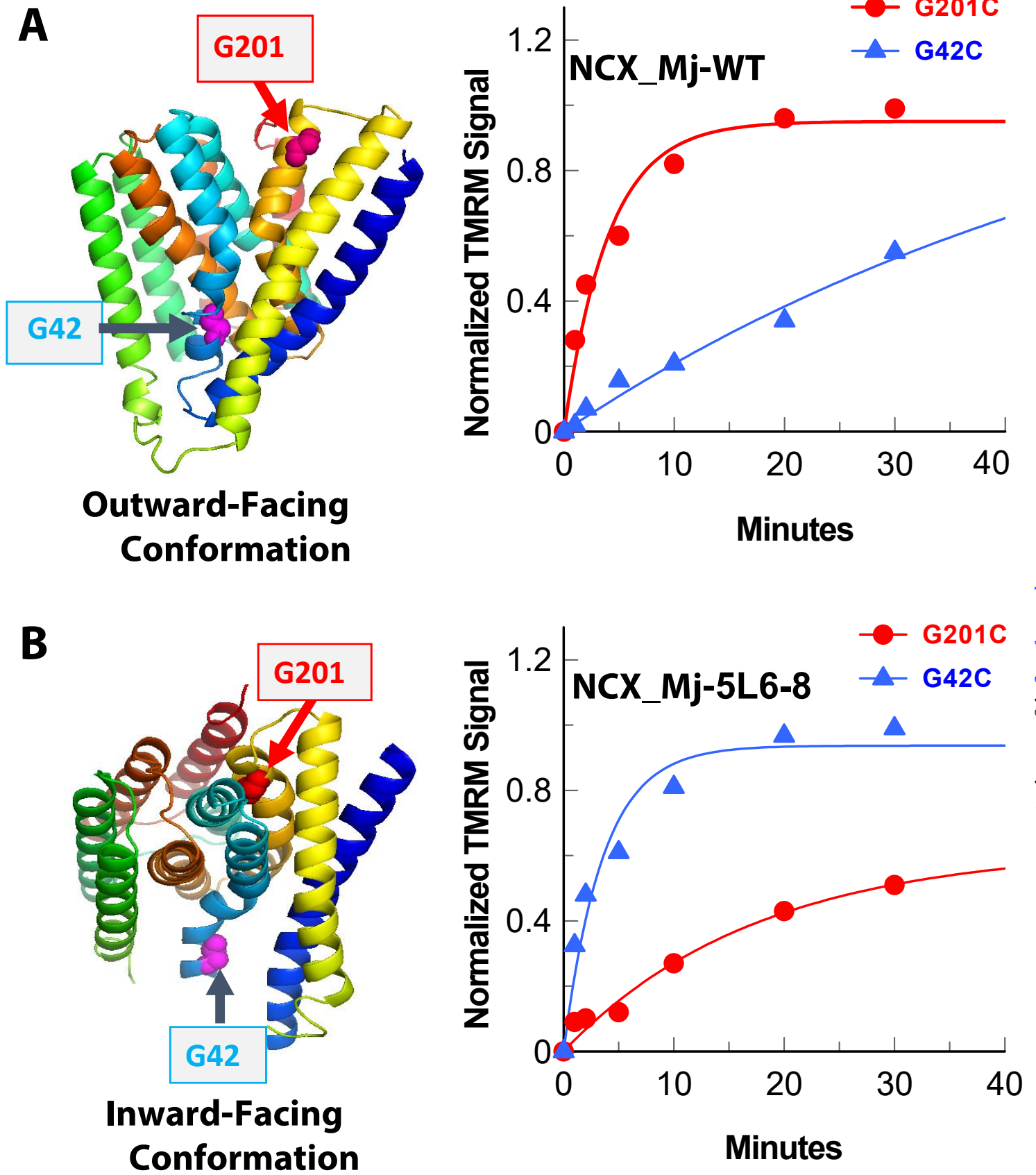


Figure 3

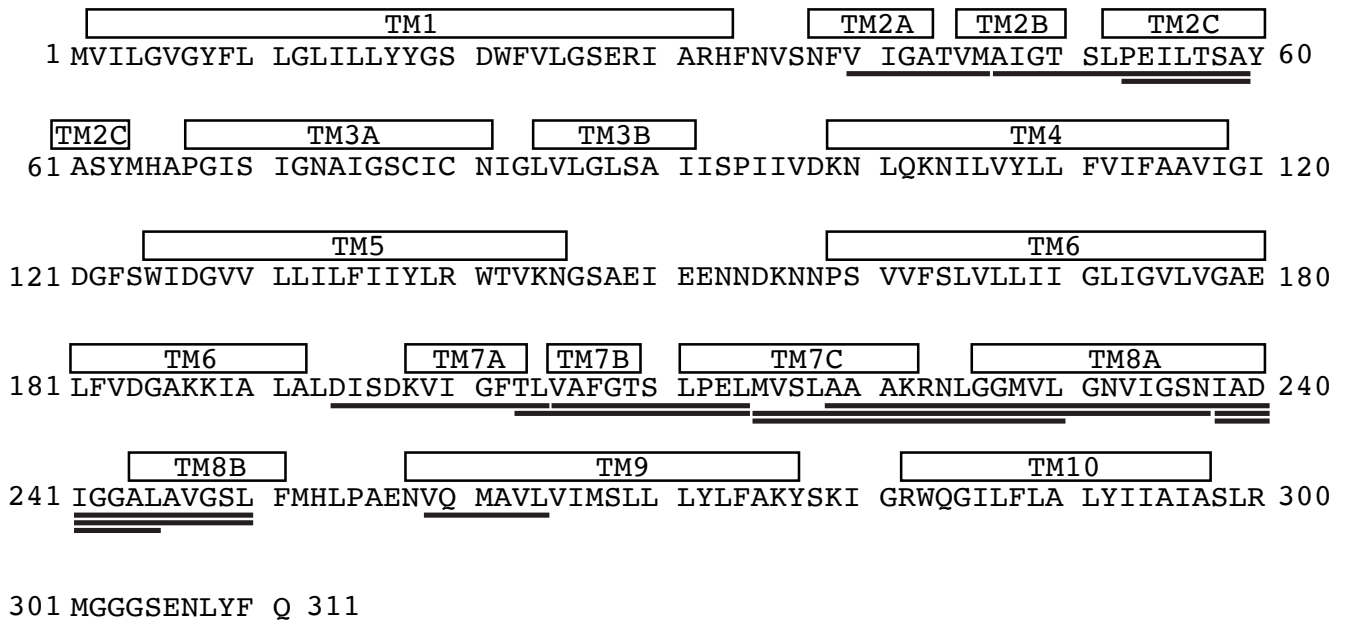


Figure 4

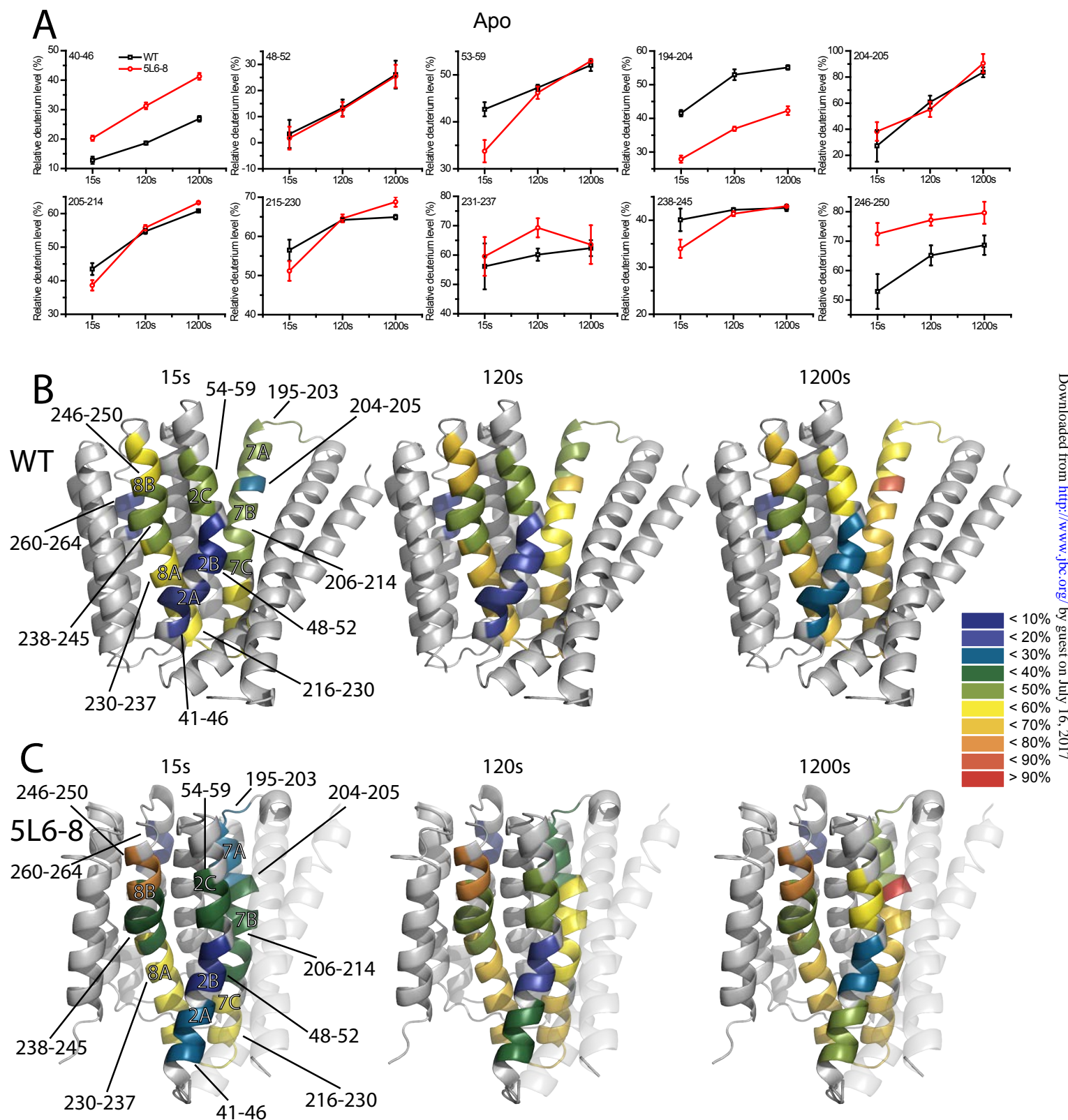


Figure 5

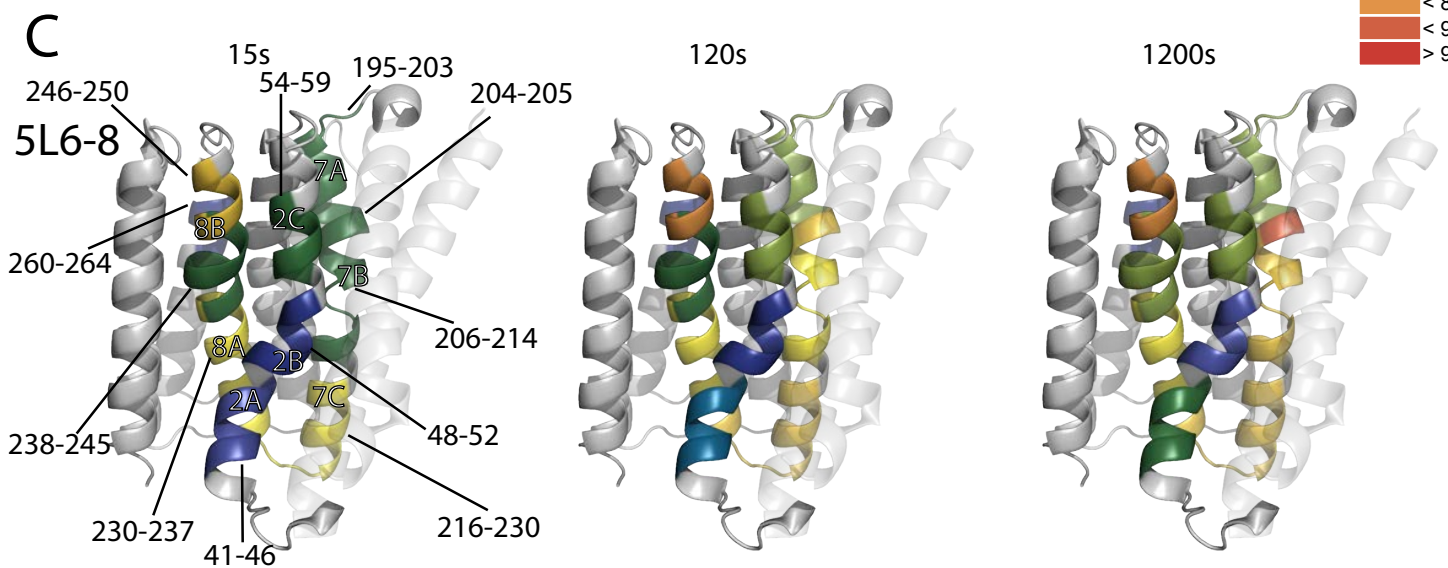
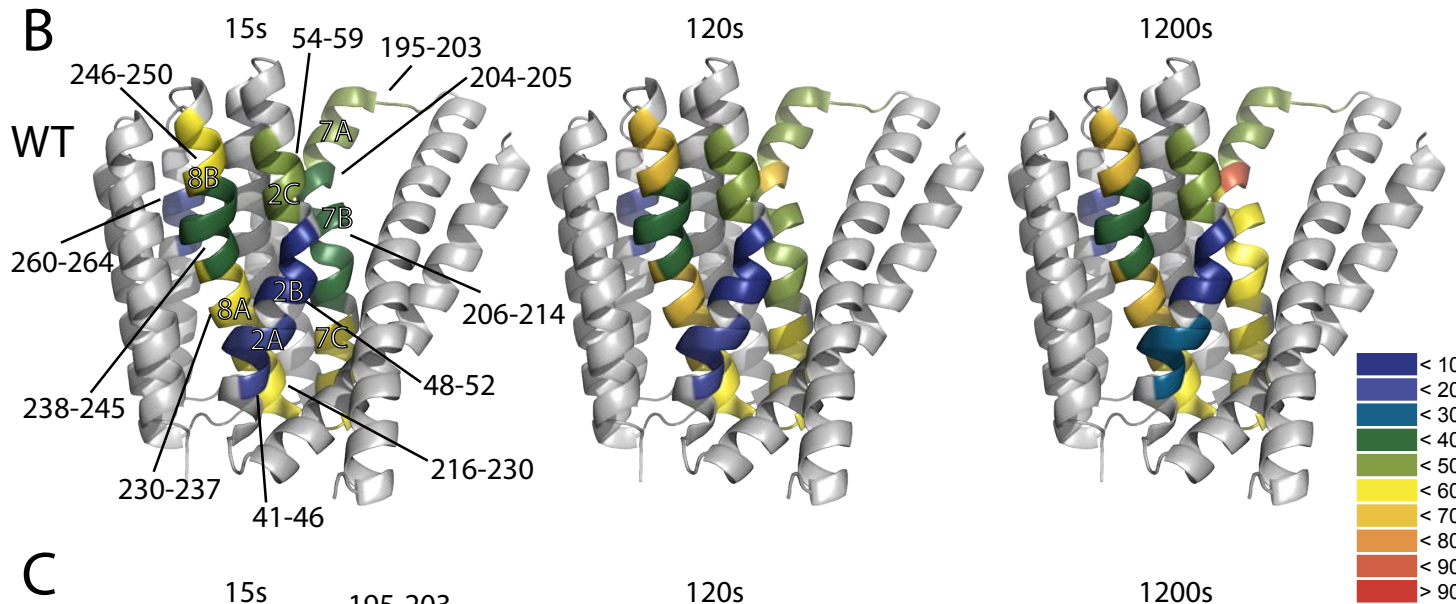
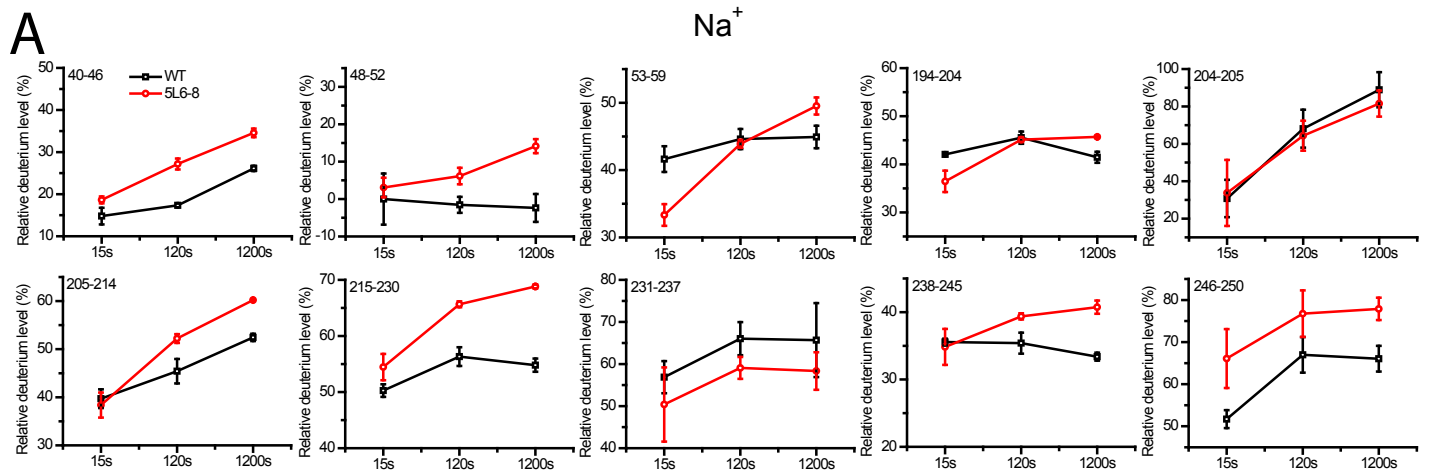


Figure 6

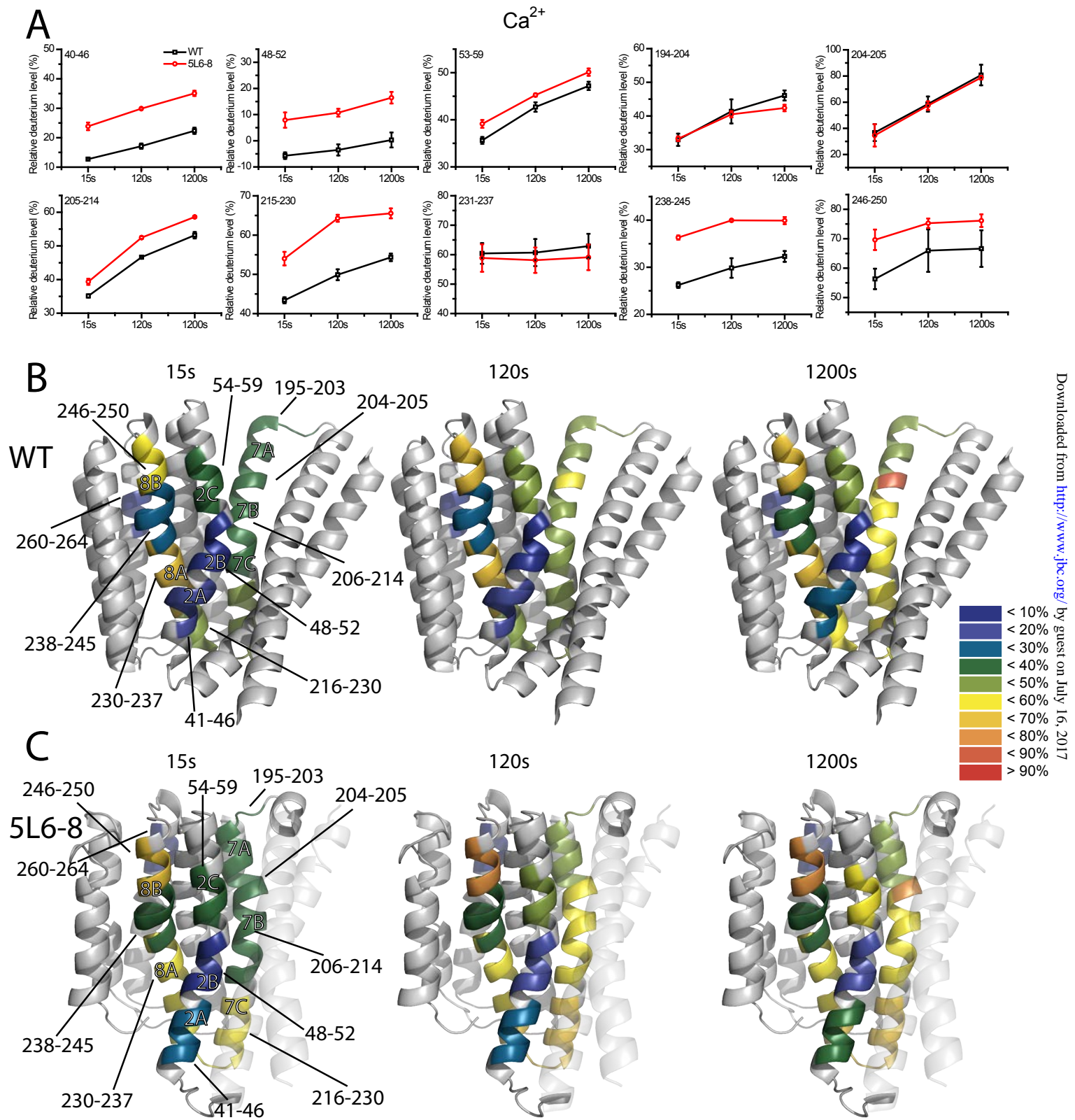


Figure 7

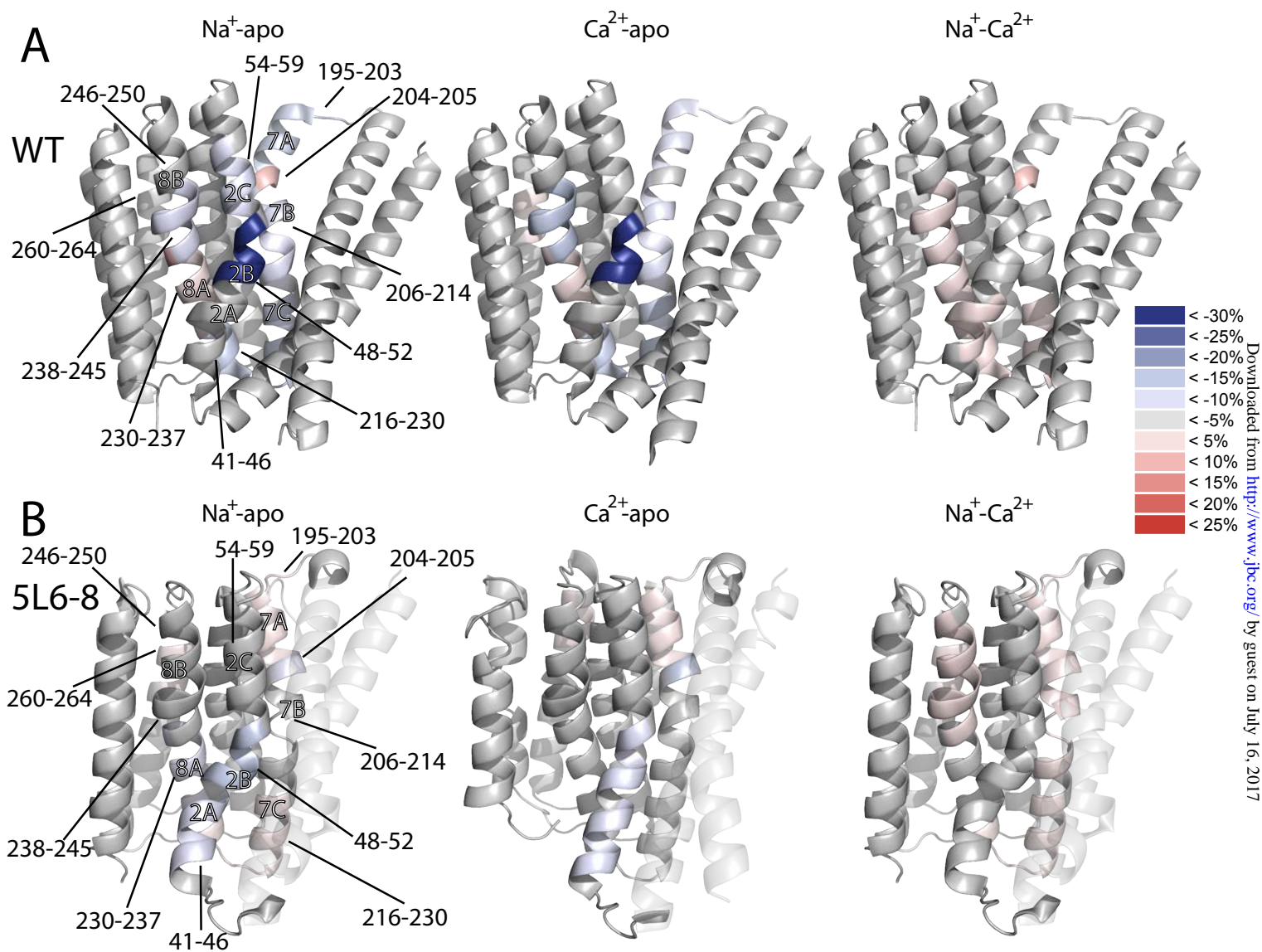


Figure 8

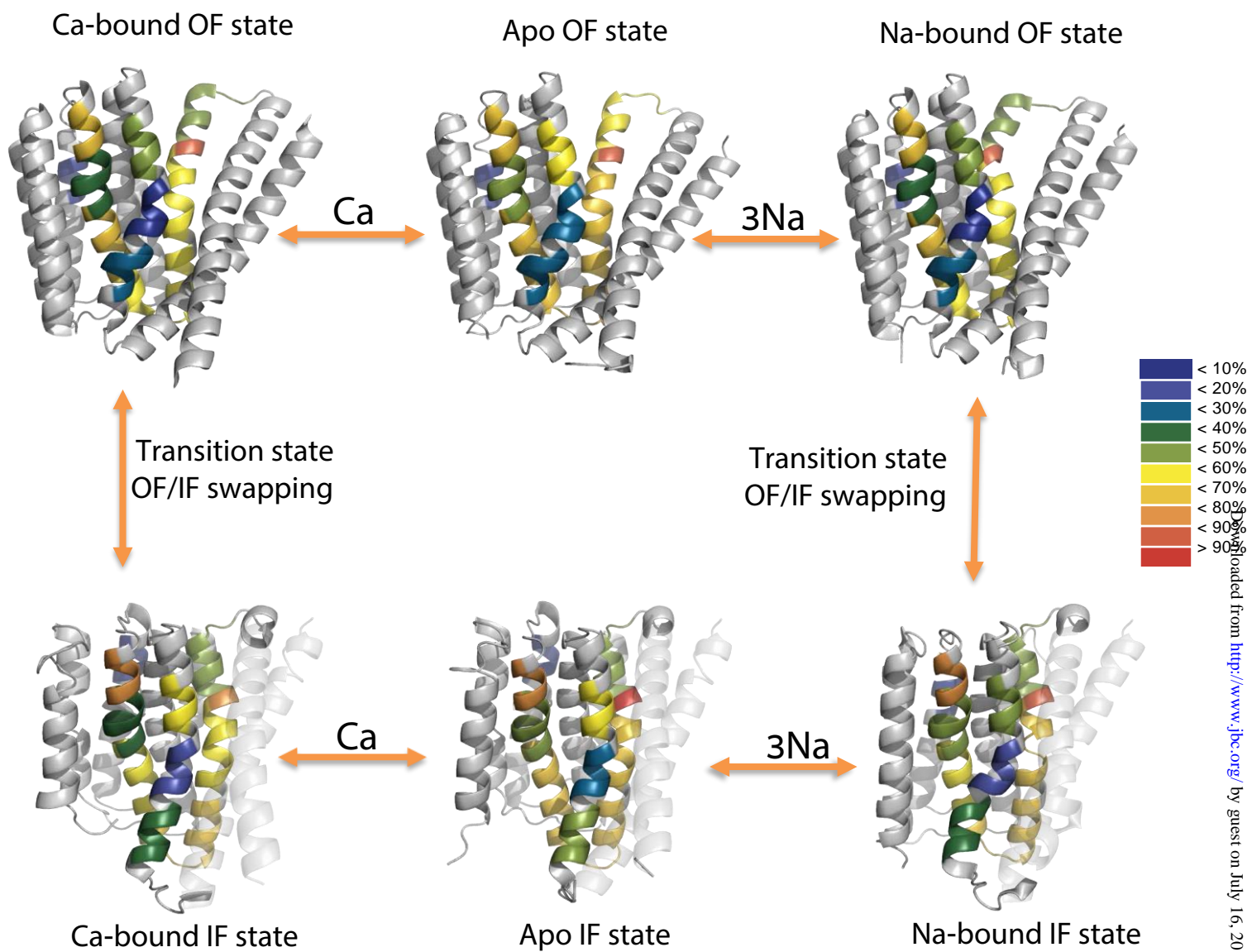
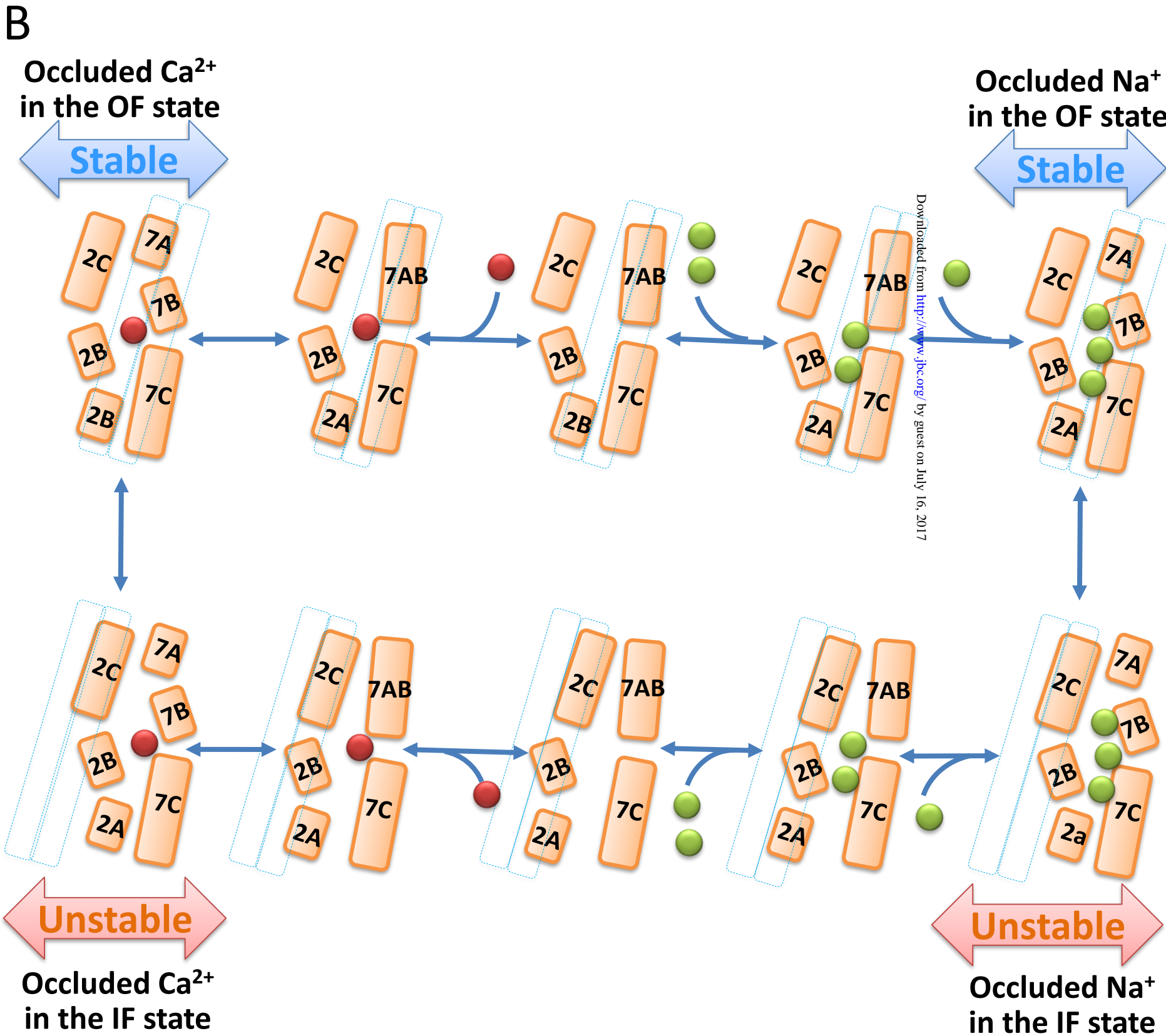
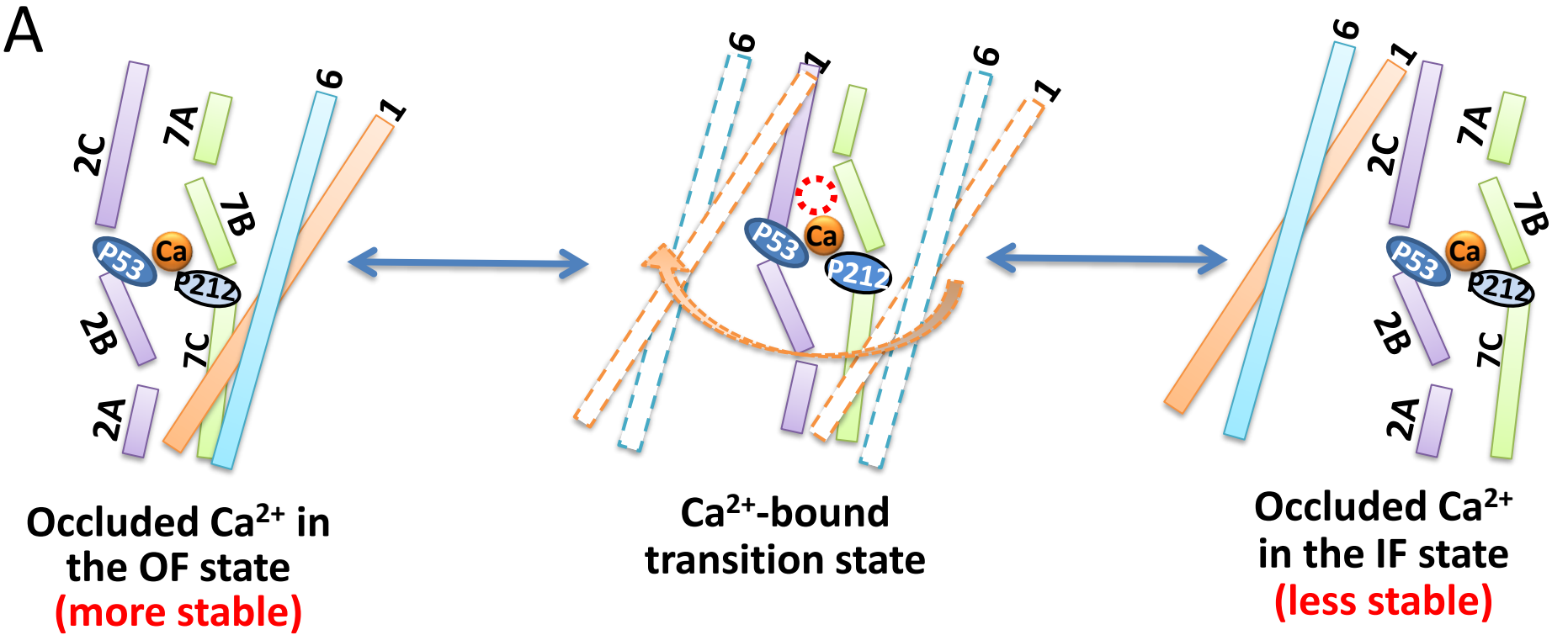


Figure 9



Dynamic distinctions in the sodium-calcium exchanger adopting the inward- and outward-facing conformational states

Moshe Giladi, Liat van Dijk, Bosmat Refaeli, Lior Almagor, Reuben Hiller, Petr Man, Eric Forest and Daniel Khananshvili

J. Biol. Chem. published online June 1, 2017

Access the most updated version of this article at doi: [10.1074/jbc.M117.787168](https://doi.org/10.1074/jbc.M117.787168)

Alerts:

- [When this article is cited](#)
- [When a correction for this article is posted](#)

[Click here](#) to choose from all of JBC's e-mail alerts

This article cites 0 references, 0 of which can be accessed free at
<http://www.jbc.org/content/early/2017/06/01/jbc.M117.787168.full.html#ref-list-1>